Forced imbibition in natural porous media: Comparison between experiments and continuum models

Amir Riaz, Guo-Qing Tang, Hamdi A. Tchelepi, and Anthony R. Kovscek
Department of Energy Resources Engineering, Stanford University, Stanford, California 94305, USA
(Received 5 September 2006; revised manuscript received 30 November 2006; published 13 March 2007)

A well-characterized set of large-scale laboratory experiments is presented, illustrating forced imbibition displacements in the presence of irreducible wetting phase saturation in a cylindrical, homogeneous Berea sandstone rock. Experiments are designed to operate in the regime of compact microscopic flows and large-scale viscous instability. The distribution of fluid phases during the flow process is visualized by high-resolution computed tomography imaging. Linear stability analysis and high-accuracy numerical simulations are employed to analyze the ability of macroscopic continuum equations to provide a consistent approximation of the displacement process. The validity of the equilibrium relative permeability functions, which form the basis for the continuum model, is fundamentally related to the stability of the displacement process. It is shown that not only is the stable flow regime modeled accurately by existing continuum models, but the onset of instability as well as the initial unstable modes are also determined with reasonable accuracy for unstable flows. However, the continuum model is found to be deficient in the case of fully developed unstable flows.

DOI: 10.1103/PhysRevE.75.036305 PACS number(s): 47.55.−t, 47.20.Ma, 47.10.ab

I. INTRODUCTION

Two-phase flow of immiscible fluids in porous media is a pore-scale process where the fluid movement at the microscopic level is governed by the flow rate, interfacial tension, wettability conditions, and random distribution of pore geometry and size [1,2]. The relative importance of capillary, viscous, and gravitational forces, which act on a large number of sharp interfaces separating the fluids, determine the overall flow characteristics. Large values of the capillary or Bond number indicate the dominance of viscous or gravitational forces, leading to the pore-scale instability regime [3–5]. On the other hand, large capillary forces, for vanishing values of the capillary or Bond number, give rise to the regime of invasion percolation [6,7]. Both regimes, which are characterized by fractal spaces, produce flow features that are on the order of the pore length; which essentially precludes, as yet, an effective representation of flow at a larger, macroscopic scale.

Flow processes that occur over length scales several orders of magnitude larger than the pore size represent a wide range of important physical applications dealing with geological fluid flow in natural rocks [8]. The capillary and Bond numbers for these flows fall between the limiting cases of pore-scale instability and invasion percolation [8]. For this intermediate regime, observations of a stable and compact flow structure at the pore scale, in some instances [9], indicate the possibility of a macroscopic flow model [10,11]. The extension of the single-phase Darcy's law to two-phase flow is based on the macroscopic phenomenological representation of microscopic processes, through the relative permeability parameter [12]. The applicability of the macroscopic framework depends on the ability of relative permeability to account accurately for pore-scale mechanisms as well as large-scale features in the flow.

Experimental observations suggest that drainage, which is the displacement of a wetting fluid by a nonwetting fluid, is unstable at the pore scale as well as the macroscopic scale, for a wide range of parameters [13–15]. On the other hand, the reverse process of imbibition is considered to be stable at the pore scale for the same set of parameters; hence, it may be modeled by a macroscopic formulation [13,16]. Imbibition processes are further classified on the basis of either the presence or the absence of irreducible wetting phase saturation. The former are observed to be highly unstable at the macroscopic level [15–17] while the latter have not been investigated from the point of view of macroscopic stability [18].

Our investigation deals with imbibition-type displacements in the presence of irreducible wetting phase saturation. Within this class of two-phase flows, the applicability of Darcy's model may be limited to cases where the macroscopic displacement is stable. However, in order to determine the applicability, as well as to understand the limitations of the continuum model, rigorous comparison between experiments and the continuum model is required, which does not exist at present. Because Darcy's law for two-phase flow serves as the basis for all geological flow models [19,20], this gap in knowledge is a serious impediment to an accurate characterization of field-scale processes.

The objectives of this investigation are, first, to provide a clear visualization of large-scale unstable displacements in real porous media along with their dependence on the capillary number and the viscosity ratio; second, to evaluate the accuracy of the stability analysis, based on experimentally determined relative permeability functions, in terms of the onset and the initial modes of instability; and finally, to examine and compare the results obtained from the well known Buckley-Leverett analytical model and high-accuracy nonlinear simulations with the experimental saturation profiles for the fully developed flow.

Either previous investigations did not attempt to evaluate the experiments in terms of the continuum model at all [9,14,18,21], or the experiments were not classified on the basis of stability and compared with the predictions of the continuum model [22–24]. As a result, comparison of stabil-

TABLE I. Properties of experimental fluids.

Phase	Fluid	Viscosity (cP)	Density (g/cm^3)
Water	8% NaBr in distilled water	1.0	1.04
Oil	nC_{10}	0.97	0.73
Oil	nC_{10} and Blandol	10.1	0.78
Oil	Blandol	27.7	0.83
Oil	Drakeol	155.0	0.87
Oil	Avatech 550	303.0	0.89

ity predictions with experimental results is missing. Attempts to simulate numerically, unstable two-phase flows have been largely unsuccessful in the past due to the lack of appropriate numerical methods [23]. Moreover, previous efforts, by disregarding capillary dispersion, suffered from spurious grid-dependent flow structures [25]. Most importantly though, simulations based on experimentally determined relative permeability functions have not been compared directly with actual unstable displacements.

We therefore perform experiments in a homogeneous Berea sandstone core, in the regimes of both stable and unstable displacements, to determine the conditions under which the macroscopic formulation is justified. We also highlight the limitations of the continuum model and attempt to build a qualitative understanding of this deficiency in order to establish a basis for further improvements in the existing model.

II. EXPERIMENTS

Imbibition experiments are performed at a constant rate in a cylindrical Berea sandstone core in the presence of an irreducible wetting phase or "connate water" saturation. Saturation distributions are obtained with the computed tomography (CT) scan procedure described below. A strongly water-wet Berea sandstone core is selected to eliminate, as much as possible, the effects of spatial variation in wettability. The test sample is also required to be homogeneous with respect to porosity and permeability, so that fundamental flow mechanisms are analyzed without interference from heterogeneity. These properties ensure repeatability of the experiments.

Experiments were carried out by injecting the "water" phase, 8% NaBr solution. Five mineral oils with different viscosities were used as the displaced "oil" phase. Properties of the experimental fluids are listed in Table I. The viscosity ratio is defined as $M=\mu_o/\mu_w$. All experiments were carried out at room temperature. Gravity effects do not come into play due to the small density difference noted in Table I. Many of the experiments were repeated and similar results were obtained, providing confidence regarding homogeneity and uniform wettability of the core.

A. Visualization method

High-resolution images of the cross sections along the test sample were obtained with CT scans. The computed tomography scanner is a fourth-generation Picker 1200SX with a scan resolution (i.e., voxel size) of $0.35\times0.35\times5$ mm^3.

The raw data obtained from the scanner are expressed as a number χ, which is a measure of the degree of x-ray attenuation by the material. The raw χ data are processed voxel by voxel to obtain the porosity and the wetting phase saturation. The porosity ϕ is obtained as

$$\phi = \frac{\chi_{wr} - \chi_{ar}}{\chi_w - \chi_a}, \tag{1}$$

where the subscripts *wr* and *ar* refer to water-filled and air-filled rock, respectively, while *w* and *a* refer to bulk water and air phases, respectively. The water saturation S_w in a cross-sectional image is obtained as

$$S_w = \frac{\chi_{wr} - \chi_{owr}}{\phi(\chi_w - \chi_o)}, \tag{2}$$

where *owr* is the oil-water phase in the rock and *o* is the oil phase. More details on CT imaging are available elsewhere [26,27].

B. Properties of Berea sandstone

The cylindrical Berea sandstone core has length $L=52$ cm and diameter $D=5.1$ cm. The aspect ratio of the sample $Y=D/L$ is about 0.1. A three-dimensional experimental sample is required to preserve the connectivity of the pore space. Average values of porosity and permeability are 20.5% and 377 mD, respectively. Local porosity measurements made with the CT scanner were found to be uniform with a spread of ±0.03 around the independently measured average porosity of 20.5%. Permeability values were obtained from the theory of constant-area stream tubes [27], based on the local porosity distribution and the travel time of the front between measurement points. The variance of permeability in this case is $O(10^{-4})$. These small variations in porosity and permeability values show that the selected core is practically homogeneous.

C. Initial conditions

The irreducible wetting phase saturation was established by first injecting the water phase into a clean, dry evacuated core to obtain 100% water saturation. Water was then displaced by injecting oil until no more water was produced at the outlet end. The procedure was carried out for each oil to determine the dependence of connate water saturation on the viscosity ratio.

Figure 1 shows water saturation at the initial condition for different values of the viscosity ratio M. Values of saturation, averaged over various cross sections, are plotted along the length of the core and are found to be closely centered around the connate water saturation $S_{wi}\approx0.3$. The dimensionless length is scaled by the total length of the sample. Figure 1 also plots the saturation level obtained at the end of the displacement experiment, which is the residual oil saturation, $S_{or}\approx0.4$. The displacement of oil through water injection takes place for saturations $S_{wi}\leqslant S_w\leqslant 1-S_{or}$.

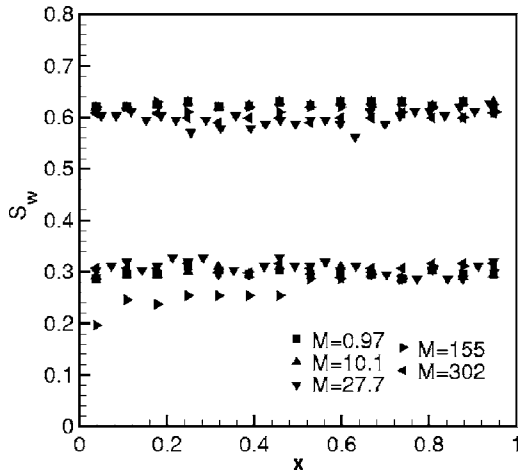

FIG. 1. Cross-sectional averages of saturation plotted along the dimensionless length of the sample. Initial conditions around $S_w = S_{wi} \approx 0.3$ show the connate water saturation while the maximum values at $S_w = 1 - S_{or} \approx 0.6$ indicate the residual oil saturations. Data for different viscosity fluids form a uniform distribution around S_{wi} and S_{or}.

D. Displacement experiments

Imbibition experiments were performed starting from the initial conditions described above. Three injection rates were used, $q = 0.5$, 1.5, and 3.0 cm^3/min, corresponding to capillary numbers of 3×10^{-7}, 9×10^{-7}, and 18×10^{-7}, where the capillary number $\mathrm{Ca} = \mu_w U / \gamma$ is based on the viscosity of the injected fluid and the injection velocity $U = 4q / \pi D^2$. The value of the interfacial tension, γ, was measured to be ≈ 40 dynes/cm for all fluid pairs.

Figure 2 plots the cross-sectional average of water saturation along the length of the core, at dimensionless time $t \approx 0.2$, for different viscosity ratios with $q = 1.5$ cm^3/min

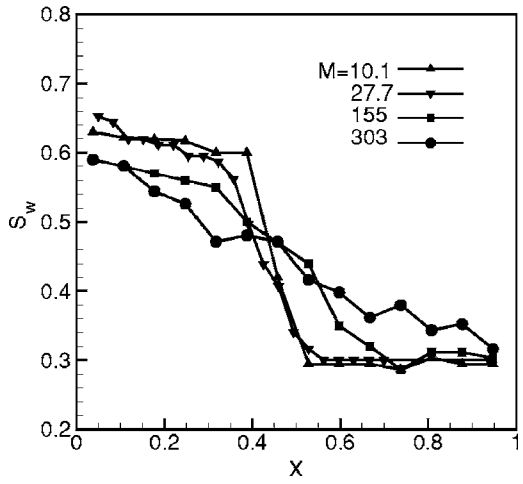

FIG. 2. Average saturation along the core during the displacement experiment for different values of M with $q = 1.5$ cm^3/min, at $t \approx 0.2$. $M = 10.1$ and 27.7 cases have relatively uniform fronts between the maximum and the minimum saturation. Larger values of M lead to significantly dispersed and irregular transition zones, indicating the existence of hydrodynamic instability.

($\mathrm{Ca} = 9 \times 10^{-7}$). Time is made dimensionless with $U/L\phi$, where ϕ is the porosity. Saturation profiles for $M = 10.1$ and 27.7 show that oil is displaced through a relatively steep interface separating the fluids. For larger values of M, the interface becomes more dispersed and irregular over increasingly larger distances.

Figure 3 shows the three-dimensional flow profile obtained by plotting saturation distribution within cross sections along the length of the core at $t \approx 0.1$. Noise in the image obtained from the CT scanner is removed by applying a high-frequency filter, with a wave number threshold equal to half the scanner resolution. Dark areas indicate the water phase while lighter regions represent oil. Contours are plotted at $S_w = 0.45$. A nonuniform invasion of water into the oil phase indicates the presence of macroscopic viscous instability. The influence of the capillary number is shown in Figs. 3(a) and 3(b) for $M = 155$. Both the number and the amplitude of the fingers increase for $q = 1.5$ cm^3/min as compared to $q = 0.5$ cm^3/min. A similar influence due to an increase in the viscosity ratio is observed by comparing Figs. 3(a) ($M = 155$) and 3(c) ($M = 303$), at $q = 0.5$ cm^3/min. The dispersed nature of the average saturation profiles in Fig. 2, is related to the generation of large-scale viscous fingers. Displacements at $M = 0.97$ and 10.1, which are not shown, were observed to be stable for all injection rates, while those at $M = 27.7$ were mildly unstable.

III. MATHEMATICAL MODEL

According to Darcy's law for two-phase flow, phase velocities are expressed as [28,29],

$$\mathbf{u}_w = -\frac{kk_{rw}}{\mu_w} \nabla P_w - \frac{kk_{rc_1}}{\mu_o} \nabla P_o, \tag{3}$$

$$\mathbf{u}_o = -\frac{kk_{ro}}{\mu_o} \nabla P_o - \frac{kk_{rc_2}}{\mu_w} \nabla P_w, \tag{4}$$

where the subscripts w and o refer to the water and oil phases, respectively. The phase viscosities are μ_w and μ_o and phase pressures are P_w and P_o. The relative permeabilities for the water and the oil phases, k_{rw} and k_{ro}, respectively, are fractions of the absolute permeability k but do not vary linearly with S_w.

The condition of mass conservation of each phase is expressed as

$$\frac{\partial S_w}{\partial t} + \nabla \cdot \mathbf{u}_w = 0, \tag{5}$$

$$\frac{\partial S_o}{\partial t} + \nabla \cdot \mathbf{u}_o = 0, \tag{6}$$

with additional constraints

$$P_o - P_w = P_c, \tag{7}$$

$$S_w + S_o = 1, \tag{8}$$

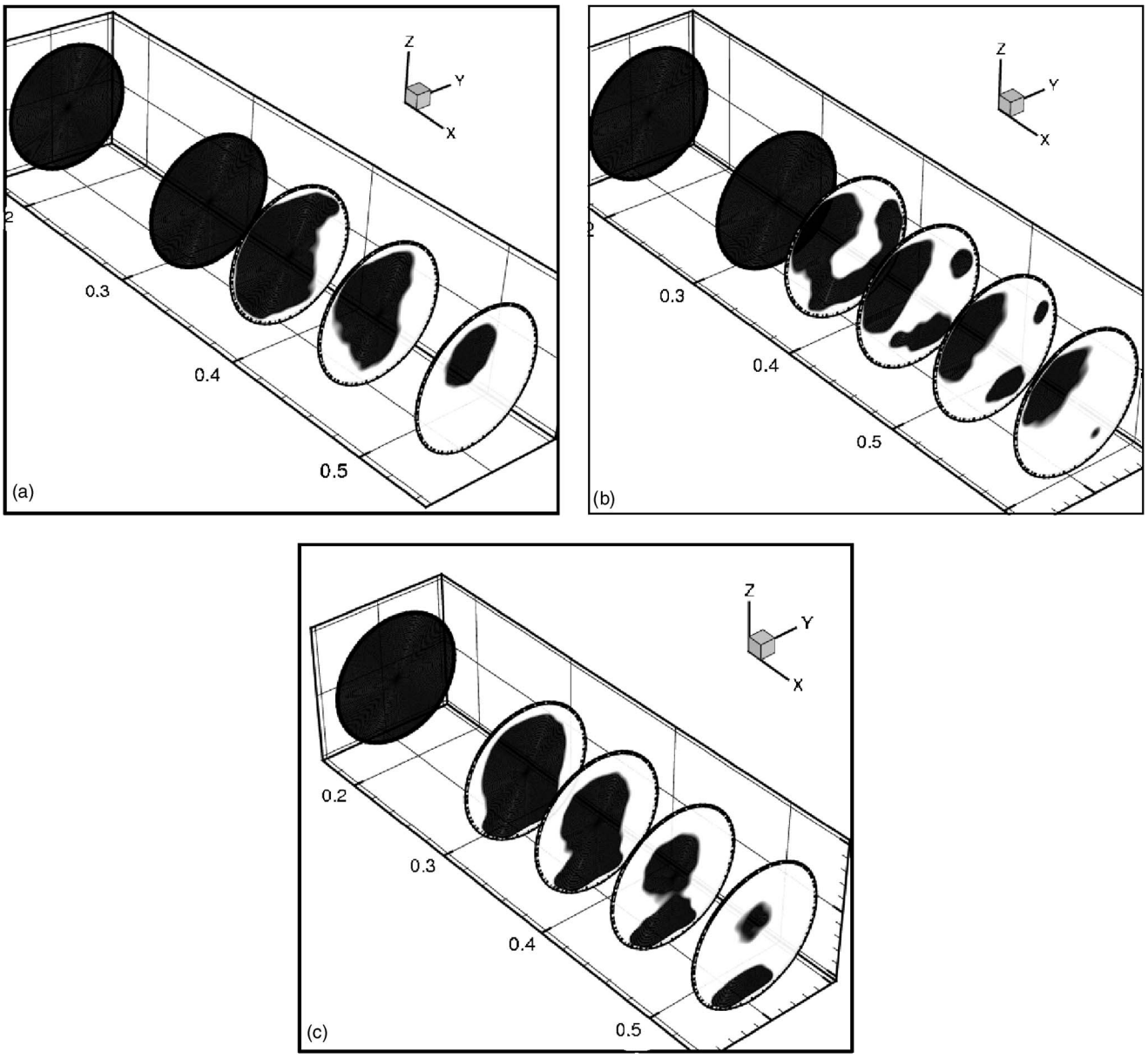

FIG. 3. Three-dimensional representation of the displacement at $t \approx 0.1$. (a) $M=155$, $q=0.5$; (b) $M=155$, $q=1.5$; and (c) $M=303$, $q=0.5$. Viscous instability develops at these values of M and more unstable structures are produced at greater M and q. Contours are plotted at $S_w=0.45$.

$$\mathbf{u}_w + \mathbf{u}_o = \mathbf{u}. \tag{9}$$

Here P_c is the capillary pressure and $\mathbf{u}$ is the total velocity. The incompressibility condition requires $\nabla \cdot \mathbf{u}=0$.

Empirical estimation is required for both the relative permeability and the capillary pressure. However, we limit experimental measurements to relative permeability only [26], because the dependence of capillary pressure on interfacial tension and water saturation is well characterized for Berea sandstone [30]. Cross-coupling terms in Eqs. (3) and (4) are neglected for small values of Ca [31]. We base our analysis on steady-state relative permeability; other methods, based on pore network models [32], lattice Boltzmann simulation [33], and theoretical analysis [31,34] suggest avenues for exploring the dynamic relative permeability tensor. These must be distinguished from the so-called dynamic measurements [35] based on displacement experiments, that lump pore-scale and macroscopic effects in a single parameter and hence suffer from the scale dependence of the measurement [24].

Figure 4 plots the steady-state relative permeability as a function of water saturation S_w for various viscosity ratios, where k_{rw} and k_{ro} are scaled by the respective maximum values $k_{rw}^{*}=k_{rw}(1-S_{or})$ and $k_{ro}^{*}=k_{ro}(S_{wi})$. These values are listed in Table II. Profiles of relative permeability functions are observed to be somewhat influenced by M.

A. Analytical solution

In the absence of variation in absolute permeability, a one-dimensional (1D) solution [19] is obtained through the

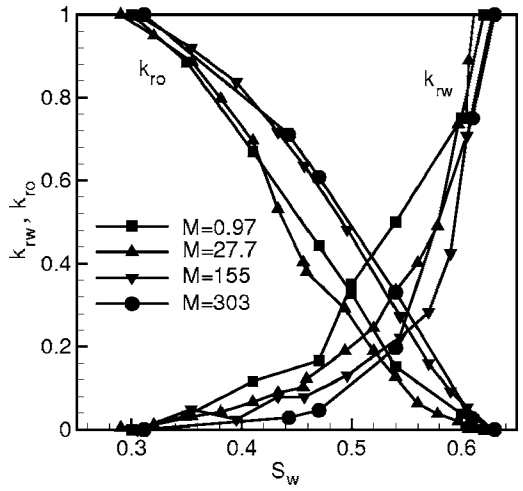

FIG. 4. Relative permeability vs water saturation, for the water and the oil phases measured under steady-state conditions at different values of M.

Buckley-Leverett (BL) formulation [36], neglecting capillary pressure and the cross-coupling terms in Eqs. (3) and (4). By considering the dimensionless velocity of the water phase as the fractional flow function f_w,

$$f_w = \frac{mk_{rw}(S_w)}{mk_{rw}(S_w) + k_{ro}(S_w)}, \tag{10}$$

the mass conservation equation of the water phase is expressed as

$$\frac{\partial S_w}{\partial t} + \frac{\partial f_w}{\partial x} = 0, \tag{11}$$

where time and length are made dimensionless with $U/L\phi$ and L, respectively. The mobility ratio m in Eq. (10) is given by $m = Mk^*_{rw}/k^*_{ro}$.

When f_w is convex, the saturation front between the fluids is a shock propagating with a speed equal to $1/(1-S_{wi}-S_{or})$. On the other hand, an inflection point in the profile gives rise to a shock for $S_{wi} < S_w < S_s$ and a rarefaction wave for $S_s < S_w < 1-S_{or}$. The shock saturation S_s is defined by

$$\left.\frac{df_w}{dS_w}\right|_{S_s} = \frac{f_w(S_s) - f_w(S_{wi})}{S_s - S_{wi}}, \tag{12}$$

and the shock velocity v_s is

TABLE II. Viscosity ratio, mobility ratio, and shock mobility ratio as given by Eq. (20). Instability occurs for $\lambda_s > 1$. End point values of relative permeability are also listed.

$M=\mu_o/\mu_w$	$m=Mk^*_{rw}/k^*_{ro}$	λ_s	k^*_{rw}	k^*_{ro}
0.97	0.07	0.07	0.07	0.85
10.1	0.1	0.26	0.049	0.83
27.7	2.0	0.98	0.045	0.79
155.0	7.12	1.84	0.035	0.78
303.0	24.23	2.12	0.06	0.74

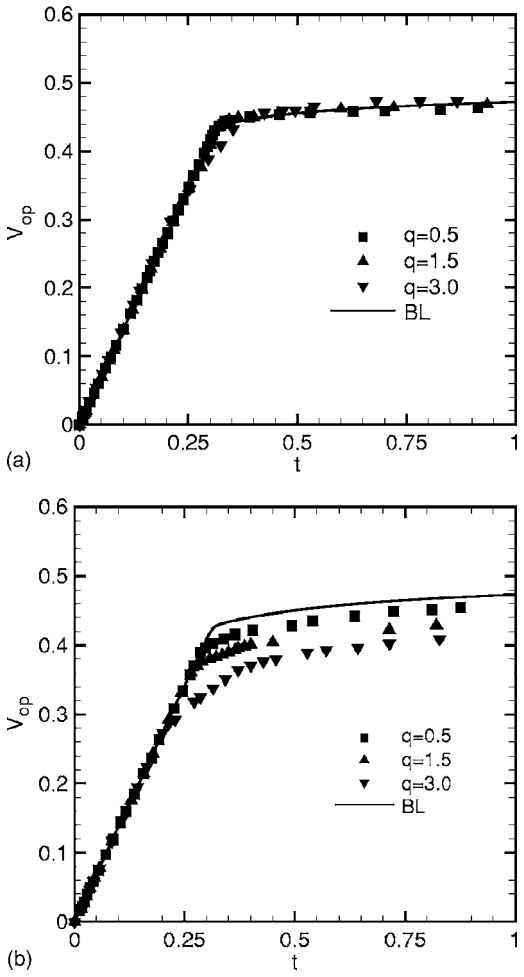

FIG. 5. Production of oil, measured as a fraction of total oil in the core, as a function of time. Plots are for $M=27.7$ (top) and 155 (bottom). Results from the Buckley-Leverett solution, shown by the solid line, deviate from experimental results at $M=155$.

$$v_s = \frac{f_w(S_s) - f_w(S_{wi})}{S_s - S_{wi}}. \tag{13}$$

The solution of Eq. (11), in terms of the location $x(t;S_w)$ for any saturation S_w, is

$$x(t;S_w) = \begin{cases} v_s t, & S_w \leqslant S_s, \\ \dfrac{df_w}{dS_w} t, & S_w > S_s. \end{cases} \tag{14}$$

Figure 5 plots the normalized cumulative oil production, V_{op}, as a function of dimensionless time for various values of M and Ca. The BL solution plotted in Fig. 5 shows good agreement with experimental results for $M=27.7$ for all injection rates, but deviates for $M=155$. In view of the stability behavior, we find that the Buckley-Leverett solution is an accurate approximation of experimental results when viscous instability is absent or mild. On the other hand, the 1D model deviates from the actual solution for unstable flows. Two-dimensional simulations with capillarity will be carried out to determine how much of the unstable behavior can be resolved with the equilibrium relative permeability functions.

But first we carry out a linear stability analysis to determine the onset conditions and obtain growth rates and wave numbers of unstable flows.

IV. STABILITY ANALYSIS

The dimensionless equations governing the stability behavior, in a frame of reference $\xi=x-v_s t$ moving with the shock velocity v_s, are [37]

$$\frac{d}{d\xi}(\bar{k}_{ro}p' + \bar{k}'_{ro}\bar{P}'_o s - v_s s) = n^2 \bar{k}_{ro} p - \sigma s, \tag{15}$$

$$\frac{d}{d\xi}\{\bar{\lambda}_T p' + \bar{\lambda}'_T \bar{P}'_o s\} - \frac{1}{\mathrm{Ca}^*}\frac{d}{d\xi}\left\{\frac{d}{d\xi}(\bar{k}_{rw}\bar{P}'_c)s\right\} = n^2 \bar{\lambda}_T p - \frac{n^2}{\mathrm{Ca}^*}\bar{k}_{rw}\bar{P}'_c s, \tag{16}$$

with boundary conditions $p=0$, $s=0$ and $p'=0$, $s'=0$ at $\xi=\pm\infty$. $\lambda_T = mk_{rw}+k_{ro}$, n is the wave number, and σ is the growth rate. Primes represent the derivative with respect to the base saturation $\bar{S}_w$ for $\bar{k}_{rw}$, $\bar{k}_{rn}$, $\bar{\lambda}_T$, and $\overline{P_c}$. In the case of base-state variables $\bar{S}_w$, $\bar{P}_o$ and perturbation variables s, p, the prime denotes the streamwise gradient. The pressure and saturation base states are given by,

$$\bar{S}'_w = D\{v_s(\bar{S}_w - S_{wi}) - [\bar{f}_w - f_w(S_{wi})]\}, \tag{17}$$

$$\bar{P}'_o = \frac{1}{\bar{\lambda}_T}(\bar{k}_{rw}\bar{P}'_c\bar{S}'_w - 1), \tag{18}$$

with the dispersion coefficient $D=\bar{\lambda}_T \mathrm{Ca}^*/\bar{k}_{rw}\bar{k}_{rn}\bar{P}'_c$. Boundary conditions for $\bar{S}_w$ and $\bar{P}_o$ are $\bar{S}_w=1-S_{or}$, $\bar{P}'_o=-1/\bar{\lambda}_T(1-S_{or})$ at $\xi=-\infty$ and $\bar{S}_w=S_{wi}$, $\bar{P}'_o=-1/\bar{\lambda}_T(S_{wi})$ at $\xi=+\infty$.

A macroscopic capillary number appears in the above equations, defined as

$$\mathrm{Ca}^* = \frac{U\mu_w L\Delta S}{\gamma\sqrt{k\phi}k^*_{rw}}. \tag{19}$$

We take L to be the core diameter. $\Delta S=1-S_{wi}-S_{or}$. The capillary pressure P_c is scaled with $\gamma\sqrt{\phi/k}$, where γ is the interfacial tension between the fluids. The selection of the capillary pressure function is based on data obtained for Berea sandstone [30].

By integrating Eqs. (15) and (16) across a step-function base profile, for $\mathrm{Ca}^*\to\infty$, a first-order solution is obtained as [38]

$$\sigma = n\frac{[f_w(S_s)-f_w(S_{wi})]}{S_s - S_{wi}}\left(\frac{\lambda_s - 1}{\lambda_s + 1}\right), \tag{20}$$

where $\lambda_s=\lambda_T(S_s)/\lambda_T(S_{wi})$ and $\lambda_T(1-S_{or})/\lambda_T(S_{wi})=m$. The criterion for the onset of instability is $\lambda_s>1$, rather than $m>1$. Table II gives values of m and λ_s for different values of M. Note that $\lambda_s<1$ for $M=0.97$ and 10.1 and the experiments do not display instability for these values of M. A mild instability occurs for $M=27.7$ for which $\lambda_s\approx 1$. Only for larger values of λ_s, $M=155$ and 303, does the level of instability becomes significant.

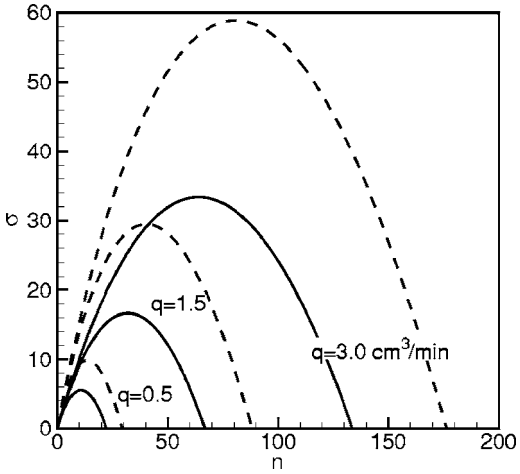

FIG. 6. Growth rate vs wave number curves for $M=155$ (solid line) and 303 (dashed line), at different capillary numbers under consideration. Maximum value of the growth rate and the corresponding most dangerous mode increase linearly with Ca^*. The maximum growth rate increases significantly when M is increased from 155 to 303 but the most dangerous mode increases only slightly.

To obtain the full unstable spectrum at finite Ca^*, we solve an algebraic eigenvalue problem [37] for the discretized form of Eqs. (15) and (16). Figure 6 shows the growth rate as a function of the wave number for $M=155$ and 303, at different values of Ca^*.

The dimensional value of the preferred unstable wavelength is obtained as $\ell=2\pi L/n_m$. The value of n_m obtained from Fig. 6 for the smallest injection rate, $q=0.5$ cm^3/min, for $M=155$ and 303 is $n_m=11.25$ and 13.8 and the preferred wavelength $\ell=2.8$ and 2.4 cm, respectively. Comparing the preferred wavelengths for $M=155$ and 303 at $q=0.5$ cm^3/min with the saturation contours close to the inlet at an early time, as plotted in Figs. 7(a) and 7(b), we observe that the width of the unstable structures is close to the estimates from the linear theory, i.e., approximately two large fingers should form. For the $M=155$ case, plotted in Figs. 7(c) and 7(d), the linear theory gives the preferred wavelengths as $\ell=0.8$ and 0.4 cm for $q=1.5$ and 3 cm^3/min, respectively. These estimates are also close to the experimental observations. The contours at late times in Figs. 7(e) and 7(f) are compared with the nonlinear simulations.

V. NONLINEAR DYNAMICS

Linear stability analysis predicts the onset of instability and also gives the preferred mode at early times with reasonable accuracy. With the help of numerical simulation, we now address the issue of the relevance of the continuum model to the fully developed experimental flow. Our high-accuracy numerical treatment of the process is based on Eq. (23), to ensure that all relevant length and time scales are properly described [39,40]. The velocity fields are computed through a stream function, with periodic boundary conditions

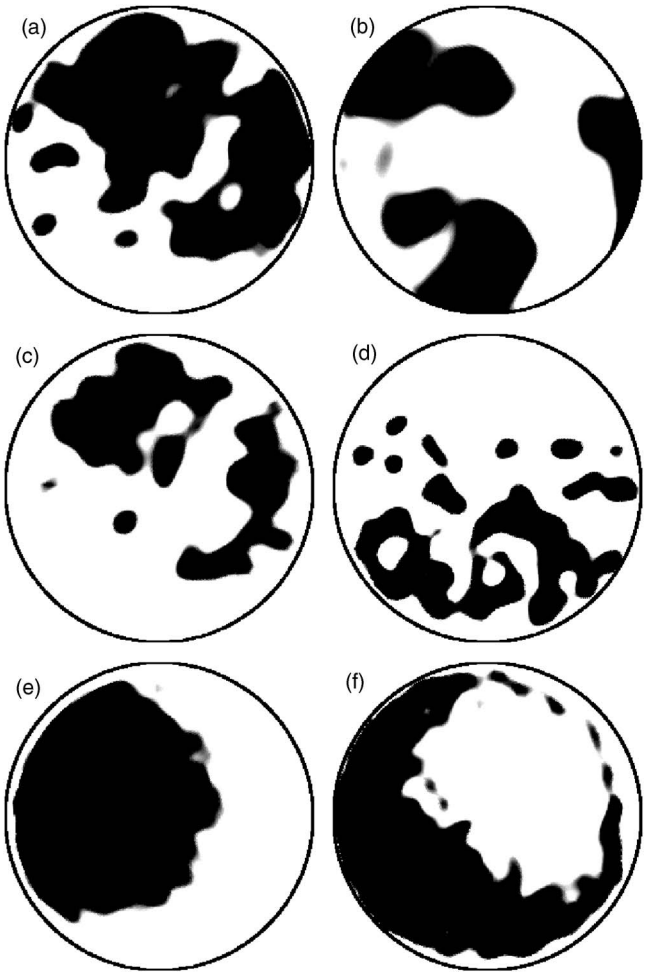

FIG. 7. Saturation contour in a cross section close to the inlet at an early time, for (a) $M=155$, $q=0.5$ cm^3/s, (b) $M=303$, $q=0.5$ cm^3/s, (c) $M=155$, $q=1.5$ cm^3/s, and (d) $M=155$, $q=3.0$ cm^3/s. (e) and (f) show contours close to the outlet at late times for $M=155$ and 303, respectively, at $q=0.5$ cm^3/s. The wavelength of unstable structures is compared qualitatively with linear stability results at early times and with nonlinear results at late times.

on saturation, vorticity, and stream function. Time integration is performed with a fourth-order Runge-Kutta method. Numerical simulations are carried out in two dimensions, because, unlike the Navier-Stokes equations, no additional flow mechanism, such as the vorticity stretching term, arise for the Darcy equations when going from the 2D to the 3D formulation [41,42].

Figure 8 plots saturation contours obtained numerically for $M=155$ and 303 with injection rates $q=1.5$ and 3.0 cm^3/min. Here, we revert to the domain length as the relevant characteristic length scale. Contours are drawn at $S_w=0.45$ for all plots. Unstable fingers are centered around the mean front. Both cases have about the same number of fingers for a given injection rate. The fingers become thinner for the higher injection rate. Linear theory predicts a much greater growth rate for $M=303$, which is reflected by a larger amplitude of fingers for this case. We obtain the nonlinear mode during the simulation as

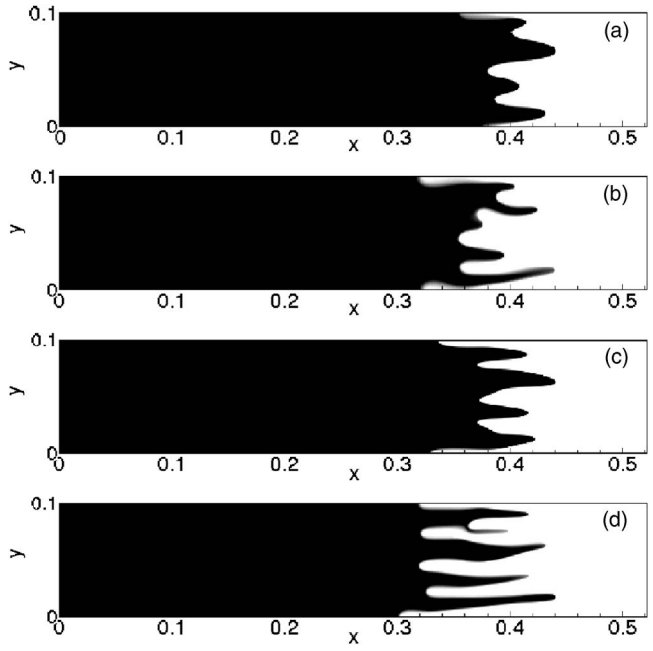

FIG. 8. Saturation contours obtained through numerical simulations. (a) $M=155$, $q=1.5$ cm^3/min, (b) $M=303$, $q=1.5$ cm^3/min, (c) $M=155$, $q=3$ cm^3/min, and (d) $M=303$, $q=3$ cm^3/min. Contours are plotted at different times for a given position of the front along the length of the domain. Unstable fingers produced for $M=303$ are slightly smaller but with a larger amplitude. The number of fingers is also in good agreement with experimental and linear stability results.

$$\hat{n}(t) = \frac{\int_0^K k\hat{\omega}(k,t)dk}{\int_0^K \hat{\omega}(k,t)dk}, \tag{21}$$

where the energy density function $\hat{\omega}$ is given by

$$\hat{\omega}^{1/2}(k,t) = \int_0^Y \left(\int_0^1 \omega(x,y,t)dx \right) e^{iky} dy, \tag{22}$$

K is the number of modes, and Y is the aspect ratio. The vorticity function ω is defined by [39]

$$\omega = \frac{1}{\lambda_T} \frac{d\lambda_T}{dS_w} \left(v\frac{\partial S_w}{\partial x} - u\frac{\partial S_w}{\partial y} \right). \tag{23}$$

The nonlinear mode is plotted in Fig. 9. At an early time, $\hat{n}$ corresponds to the most dangerous mode given by the linear analysis. At later times $\hat{n}$ undergoes significant nonlinear coarsening where the rate of decay follows an approximate scaling between $t^{-0.8}$ and $t^{-1.7}$. Note that $\hat{n}$, which includes the factor 2π in view of the transform Eq. (22), scales with the domain length such that $\hat{n}=0.2$ gives a wavelength of 0.5 in the y coordinate. The magnitude of the wave number for $q=0.5$ cm^3/min at late times is $\hat{n}\approx 0.1$, suggesting the presence of a single unstable finger. This observation is in agreement with saturation contours obtained from the experiments, as shown in Figs. 7(e) and 7(f).

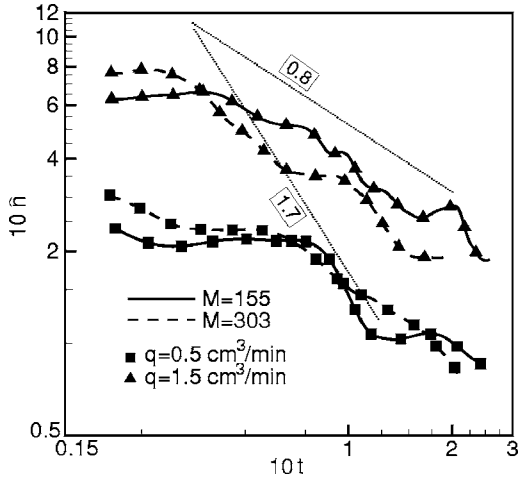

FIG. 9. Nonlinear mode during the simulation for two values each of M and Ca^*. Initially, $\hat{n}$ is close to the mode given by the linear stability results but drops rapidly to smaller values. The coarsening dynamics is governed by approximate scaling, indicated by the dotted lines, between $\hat{n} \propto t^{-0.8}$ and $t^{-1.7}$.

A more detailed comparison is presented in Fig. 10, which shows transversely averaged saturation profiles as a function of the domain length. The Buckley-Leverett solution is plotted for reference, which shows the shock at the mean front location. Cross-sectional averages are also plotted for the experiments. Numerical results show a spread of the average saturation around the mean front due to unstable fingers. Figure 10 shows that the spread obtained through numerical simulations give substantial improvement over the 1D model

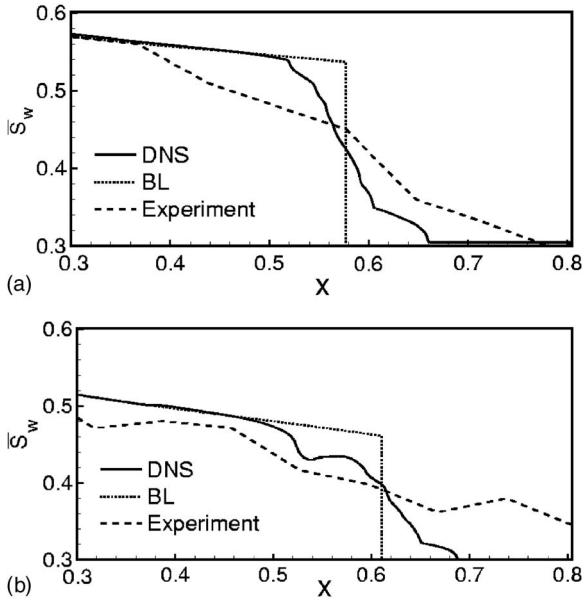

FIG. 10. Comparison of the cross-sectional average of saturation along the core length obtained with experiments and Buckley-Leverett (BL) and direct numerical simulations (DNS). (a) $M=155$, $t=0.17$ and (b) $M=303$, $t=0.14$, at $q=0.5$ cm^3/min. Saturation profile obtained from simulation shows spread around the mean position of the BL front but falls short of capturing the wider spread observed in the experiments.

but still falls short of capturing the larger spread associated with the experiments. This implies that the amplitude of unstable fingers is somewhat greater than that obtained through numerical simulations for the same set of governing parameters.

VI. DISCUSSION

Two-phase flow in porous media continues to be a source of interest from the physical as well as the engineering perspective. Despite a long history of significant research, many issues of fundamental importance remain unresolved, such as the link between the microscopic physical mechanisms and the macroscopic continuum models, as well as the role of large-scale instability. At the center of the problem is the classical phenomenological parameter of relative permeability, which is either ignored by some researchers, due to the lack of a rigorous theoretical basis [9,14,18,21], or accepted by others as a practical solution for large-scale flow problems [11,20,32,43,44]. Although a measure of theoretical rigor has been brought to bear on the problem through the theory of invasion percolation [45], the validity of equilibrium relative permeability has not been evaluated for actual large-scale flows, particularly in the presence of instability.

The present investigation seeks to establish the missing link between the pore-scale viewpoint and the practical modeling of large-scale flows, in order to determine the range of validity of the equilibrium relative permeability, which would subsequently guide future improvements in the continuum model. We find that the onset of macroscopic instability marks the threshold of the unconditional validity of the macroscopic model. However, the important point is that the onset occurs for viscosity ratios that are much larger than unity, and is determined correctly by the stability theory based on the steady-state relative permeability. This shows that relative permeability not only is valid for the trivial case of favorable viscosity ratio ($M<1$), but also is applicable over a wide range of $M>1$. Moreover, the correct determination of the onset conditions, as well as the initial unstable mode, provide confidence in the ability of steady-state relative permeability to help identify unstable displacements along with the preferred wavelength.

Although there is qualitative agreement between simulations and experiments in the nonlinear regime at late times, e.g., the nonlinear coarsening characteristics, the correct amplitude of viscous fingers is not captured by the current continuum model. The fact that the initial mode of instability is determined accurately by the use of steady-state relative permeability functions indicates that the deviation from equilibrium occurs at late times due to the formation of large-amplitude fingers. This observation is supported by the evidence of substantial vorticity generation at the finger tips [46], which creates nonequilibrium as well as viscous coupling effects at the pore scale [2,47] by giving rise to large enough local velocities. The functional form of the relative permeability functions changes under these conditions. A previous study [40] shows that both the amplitude and the mode of instability depend significantly on the functional form of the relative permeability. Hence, assumptions of cap-

illary equilibrium, negligible viscous coupling, and momentum exchange [47,48], underlie the observed discrepancy of the continuum results in the nonlinear regime.

Our analysis identifies the unstable nonlinear flow as the regime where efforts to improve the continuum model should be focused. This requires a detailed consideration of meniscus formation and displacement through the microscopic pore space, the magnitude of shear stresses across fluid-fluid interfaces, and the level of simultaneous flow through the pore spaces [49,50]. Analysis of the transient state of these mechanisms, through which capillary equilibrium is eventually established, would serve as a basis of the dynamic, or nonequilibrium, model of relative permeability. Such an undertaking involves experiments and numerical simulations at the pore scale to construct the dynamic relative permeability tensor, its consistent reduction to the equilibrium case, and the verification of the improved model through large-scale experiments and simulations. Investigation of these issues is the focus of our ongoing research.

ACKNOWLEDGMENTS

The authors gratefully acknowledge support by the SUPRI-A, SUPRI-B, and GCEP programs at Stanford University and by Chevron Technology Company. Insightful discussions with Dr. M. Kumar and Dr. J. Kamath contributed to an improved understanding of the problem.

[1] M. Blunt and M. J. King, Phys. Rev. A **46**, 7680 (1992).
[2] D. G. Avraam and A. C. Payatakes, Ind. Eng. Chem. Res. **38**, 778 (1999).
[3] K. J. Maloy, J. Feder, and T. Jossang, Phys. Rev. Lett. **55**, 2688 (1985).
[4] J. D. Chen and D. Wilkinson, Phys. Rev. Lett. **55**, 1892 (1985).
[5] R. Lenormand and C. Zarcone, J. Fluid Mech. **189**, 165 (1988).
[6] D. Wilkinson and J. F. Willemsen, J. Phys. A **16**, 3365 (1983).
[7] M. Chaouche, N. Rakotomalala, D. Salin, B. Xu, and Y. C. Yortsos, Phys. Rev. E **49**, 4133 (1994).
[8] M. Sahimi, Rev. Mod. Phys. **65**, 1393 (1993).
[9] V. Frette, K. J. Maloy, F. Boger, J. Feder, T. Jossang, and P. Meakin, Phys. Rev. A **42**, 3432 (1990).
[10] B. Xu, Y. C. Yortsos, and D. Salin, Phys. Rev. E **57**, 739 (1998).
[11] M. Blunt and P. King, Phys. Rev. A **42**, 4780 (1990).
[12] M. Muskat, J. Appl. Phys. **8**, 274 (1937).
[13] D. A. Stokes, J. P. Weitz, A. Gollub, M. O. Dougherty, P. M. C. Robbins, and H. M. Lindsay, Phys. Rev. Lett. **57**, 1718 (1986).
[14] E. J. Peters and D. L. Flock, SPE J. **21**, 249 (1981).
[15] D. Pavone, SPE Reservoir Eng. **7**, 187 (1992).
[16] P. van Meurs, Trans. AIME **210**, 295 (1957).
[17] L. Thibodeau, T. Guo, and H. N. Graham, Powder Technol. **93**, 209 (1997).
[18] J. D. Chen, M. M. Dias, S. Patz, and L. M. Schwartz, Phys. Rev. Lett. **61**, 1489 (1988).
[19] J. Bear, *Dynamics of Fluids in Porous Media* (Wiley, New York, 1972).
[20] D. Wilkinson, Phys. Rev. A **34**, 1380 (1986).
[21] V. Frette, J. Feder, T. Jossang, P. Meakin, and K. J. Maloy, Phys. Rev. E **50**, 2881 (1994).
[22] J. Kamath, B. Xu, S. H. Lee, and Y. C. Yortsos, J. Pet. Sci. Eng. **20**, 109 (1998).
[23] M. T. Vives, Y.-C. Chang, and K. K. Mohanty, SPE J. **4**, 260 (1999).
[24] E. J. Peters and S. Khataniar, SPE Form. Eval. **2**, 469 (1987).
[25] A. J. Chorin, Commun. Math. Phys. **91**, 103 (1983).
[26] J. M. Schembre and A. R. Kovscek, J. Pet. Sci. Eng. **39**, 159 (2003).
[27] E. M. Withjack, SPE Form. Eval. **3**, 694 (1988).
[28] M. Hassanizadeh and W. Gray, Adv. Water Resour. **3**, 25 (1980).
[29] S. Whitaker, Transp. Porous Media **1**, 105 (1986).
[30] P.-E. Oren and S. Bakke, J. Pet. Sci. Eng. **39**, 177 (2003).
[31] O. R. Ayodele, Transp. Porous Media **64**, 171 (2006).
[32] M. S. Al-Gharbi and M. J. Blunt, Phys. Rev. E **71**, 016308 (2005).
[33] R. D. Hazlett, S. Y. Chen, and W. E. Soll, J. Pet. Sci. Eng. **20**, 167 (1998).
[34] N. Rakotomalala, D. Salin, and Y. C. Yortsos, Appl. Sci. Res. **55**, 155 (1995).
[35] E. F. Johnson, D. P. Bossler, and V. O. Naumann, Trans. AIME **216**, 370 (1959).
[36] S. E. Buckley and M. C. Leverett, Trans. AIME **146**, 107 (1942).
[37] A. Riaz and H. A. Tchelepi, Phys. Fluids **16**, 4727 (2004).
[38] J. Hagoort, SPE J. **4268**, 63 (1974).
[39] A. Riaz, H. Hesse, H. A. Tchelepi, and F. M. Orr Jr, J. Fluid Mech. **548**, 87 (2006).
[40] A. Riaz and H. A. Tchelepi, Transp. Porous Media **64**, 315 (2006).
[41] W. B. Zimmerman and G. M. Homsy, Phys. Fluids A **4**, 1901 (1992).
[42] H. A. Tchelepi, F. M. Orr Jr, N. Rakotomalala, D. Salin, and R. Woumeni, Phys. Fluids A **5**, 1558 (1993).
[43] H. Scher and M. J. Blunt, Phys. Rev. E **52**, 6387 (1995).
[44] M. J. and Blunt, Phys. Rev. E **71**, 026301 (2005).
[45] D. Wilkinson and M. Barsony, J. Phys. A **17**, L129 (1984).
[46] A. Riaz and H. A. Tchelepi, Phys. Fluids **18**, 14104 (2006).
[47] H. Li, C. Pan, and C. T. Miller, Phys. Rev. E **72**, 026705 (2005).
[48] P. A. Goode and T. S. Ramakrishnan, AIChE J. **39**, 1124 (1993).
[49] W. Gray and M. Hassanizadeh, Adv. Water Resour. **21**, 261 (1998).
[50] M. Hassanizadeh and W. Gray, Adv. Water Resour. **16**, 53 (1993).